Preprint Title Mapping the local dielectric constant of a bio-nanostructured system

Authors Wescley W. Valeriano, Rodrigo R. Andrade, Juan P. Vasco, Angelo Malachias, Bernardo Ruegger A. Neves, Paulo Sergio S. Guimarães and Wagner N. Rodrigues

Publication Date 09 Okt. 2020

Article Type Full Research Paper

ORCID® iDs Wescley W. Valeriano - https://orcid.org/0000-0003-1181-2533; Bernardo Ruegger A. Neves - https://orcid.org/0000-0003-0464-4754; Paulo Sergio S. Guimarães - https://orcid.org/0000-0002-0113-2641; Wagner N. Rodrigues - https://orcid.org/0000-0002-6147-7799

Mapping the local dielectric constant of a bio-nanostructured system

Wescley Walison Valeriano*[1], Rodrigo Ribeiro Andrade[2], Juan Pablo Vasco[3], Angelo Malachias[1], Bernardo Ruegger Almeida Neves[1,2], Paulo Sergio Soares Guimarães[1], and Wagner Nunes Rodrigues[1,2].

[1] Departamento de Física, ICEx, Universidade Federal de Minas Gerais, Av. Antônio Carlos 6627, 31270-901 Belo Horizonte, Minas Gerais, Brazil

[2] Centro de Microscopia, Universidade Federal de Minas Gerais, Av. Antônio Carlos 6627, 31270-901 Belo Horizonte, Minas Gerais, Brazil

[3] Institute of Theoretical Physics, Ecole Polytechnique Fédérale de Lausanne EPFL, CH-1015 Lausanne, Switzerland

Email: Wescley Walison Valeriano – wescleyvaleriano@gmail.com

* Corresponding author

Abstract

The aim of this work is to determine the dielectric constant value of a bio-nanostructured system via Electrostatic Force Microscopy (EFM) and to show how this method is useful to study natural photonic crystals. We mapped the dielectric constant of the cross-section of the posterior wing of the damselfly *Chalcopteryx rutilans* with nanometric resolution and obtained not only structural information on its constitutive nanolayers but also on the absolute values of the dielectric constant variation in a nanometric scale. By relating the measured profile of the static dielectric constant to the profile of the refractive index in the visible range, combined with optical reflectance measurements and simulation, we were able to describe the origin of the strongly iridescent wing colors of this Amazonian rainforest damselfly. The method we demonstrate here should be useful for the study of other nanostructured biological systems.

Keywords

dielectric constant; electrostatic force microscopy (EFM); natural photonic crystals; relative permittivity; structural colors

Introduction

The dielectric constant, or relative permittivity, is a fundamental physical property which is crucial for describing various phenomena, either biological, chemical, or physical. It is a material property associated to the decrease of the electric force among two-point charges due to the medium. Therefore, it modulates the interaction between charged particles within materials and also the interaction of electromagnetic radiation with matter. Accordingly, it plays a fundamental role in fields as diverse as, for example, the full understanding of proteins [1,2] or in the development of solar cells [3].

Natural photonic crystals are exciting nanostructured systems in which the dielectric properties play a fundamental role [4]. Many of them are biological systems where the richness of colors, produced by different strategies found by Nature, is astonishing [5,6]. Studies of the origin of physical colors in insects are numerous in the literature and the most used tools are non-local optical reflectance, electron microscopies, and scanning probe microscopies, which give support to theoretical models aiming to describe the measured optical properties [7]. However, all these techniques directly reveal only the structure with nanometric resolution, the local dielectric response is indirectly inferred from the model [8–10]. Despite the large number of studies, the local dielectric properties of natural photonic crystals remain essentially undetermined due to the great difficulties in measuring the dielectric response at the nanometric scale [11]. The nanometric local relative permittivity of a natural photonic crystal have not been directly measured yet.

Fumagalli *et al.* [12–15], and Riedel *et al*. [16] developed several techniques of Electrostatic Force Microscopy (EFM) to extract the relative permittivity at the nanoscale, allowing new fields to be explored. Here we use EFM to map the relative

permittivity of nanostructures within the wings of the *Chalcopteryx rutilans* damselfly [17–19]; nanostructures which make it a natural photonic crystal. We obtain quantitative information about the wing structure and its local relative permittivity properties. We also simulate the optical reflectance using the extracted spatial profile of the relative permittivity and compare it with the measured reflectance in the visible range, obtaining a good correlation. In this way, we can provide a full description of the origin of the shimmering colors of the *Chalcopteryx rutilans* damselfly male posterior wings. This technique should be useful in the study of similar systems and could be included in their advanced characterization toolkit, enhancing, thus, the investigation possibilities of natural photonic crystals.

Results and Discussion

In damselflies, color has many functions, the most important being sex recognition, courtship and territory defense behaviors [19]. In *Chalcopteryx rutilans* – a damselfly found in the Amazonian rain forest – those functions are performed by the male by displaying its strongly iridescent hind wings. This phenomenon of iridescence results from physical effects such as diffraction and interference, and all observed colors result from a multilayer structure, *i.e.*, these wings are natural one-dimensional photonic crystals [7–10].

We choose three different colored regions of the iridescent posterior wings of the male *Chalcopteryx rutilans* to study – Yellow/Green, Red, and Blue regions, observed in the dorsal side, Figure 1a. The ventral side shows several shades of red, Figure 1b.

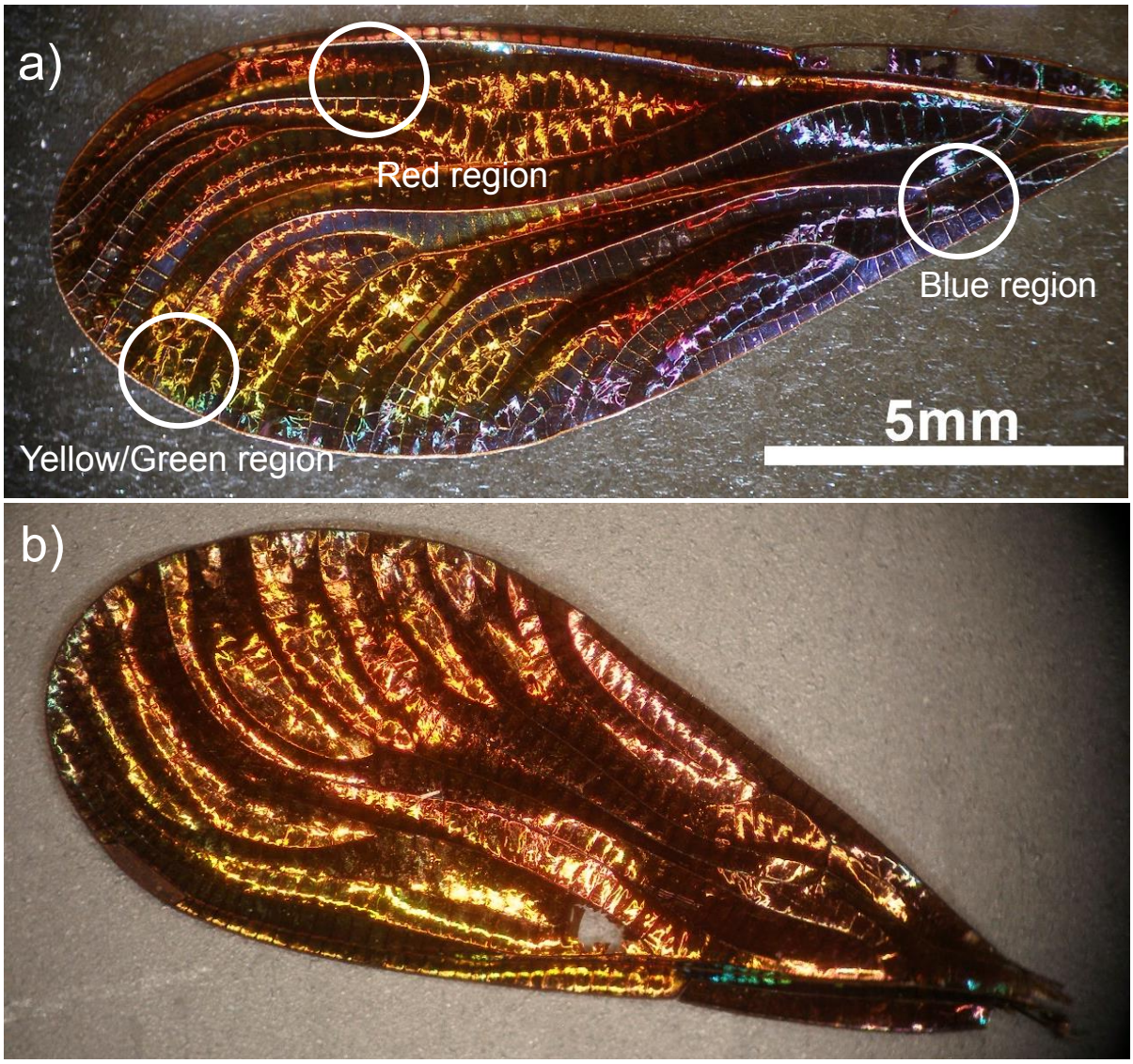

Figure 1: Optical images of the iridescent hind wing of the male damselfly *Chalcopteryx rutilans* (Rambur) (Odonata, Polythoridae). The dorsal side a) displays colors that span all the visible wavelength spectrum. The image b) shows the ventral side, which is almost all red, remarkably similar to the iridescent wing of the female *C. rutilans*.

The Scanning Electron Microscopy – SEM – image presented in Figure 2 shows the nanostructured section of a fragment of the Red region indicated in Fig.1a. The section was partially polished via Focused Ion Beam – FIB and the multilayered structure is

clearly visible. Detailed electron microscopies and mass spectrometry studies of this natural nanostructured system can be found in Valeriano [17] and Carr *et al.* [18].

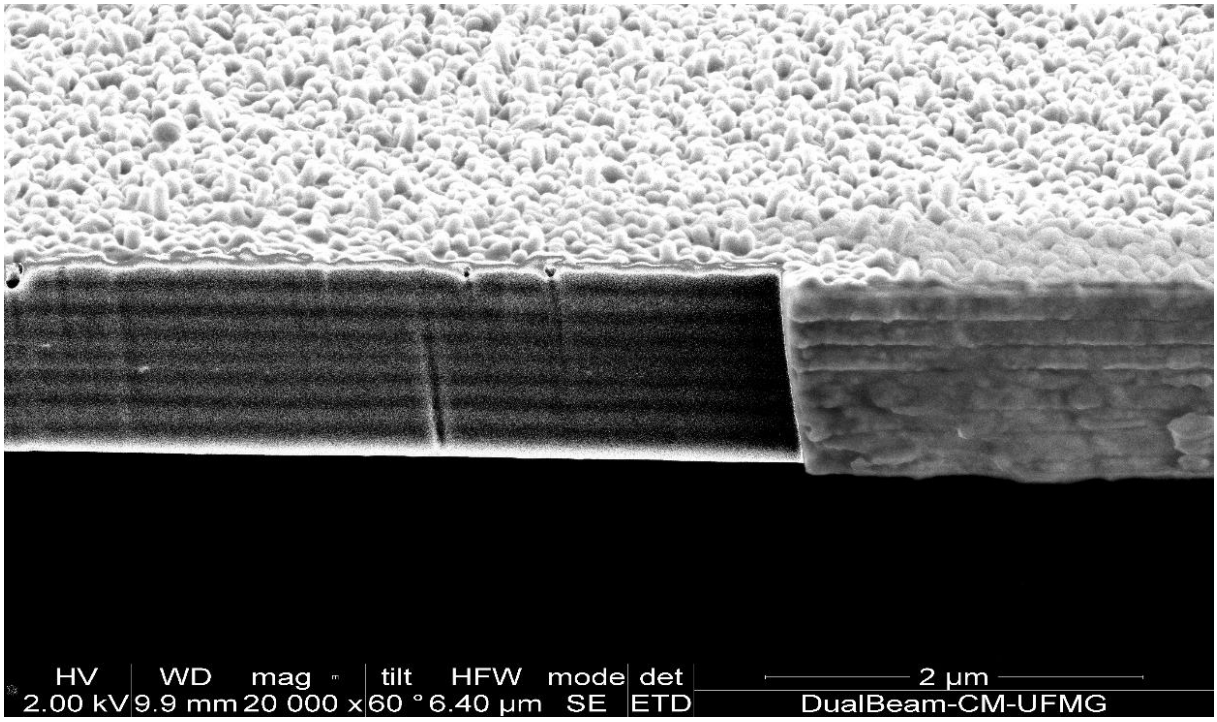

Figure 2: SEM image of the cross-section of a Red region fragment of the *Chalcopterix rutilans* male rear wing. The smooth region was obtained by polishing using FIB. The corrugated surface is the wax layer that covers the damselfly wings.

Relative permittivity determination via EFM

The EFM measurements were performed in the conventional double pass mode, which means that the probe executes two scans – the first scan measures the sample topography in tapping mode and the second scan mimics that profile at a defined lift height H_{lift} applying a voltage V_{dc} between the tip and the conductive substrate [20].

The tip is forced to oscillate, during the second pass, at the cantilever's resonance frequency, f_0. Variations in the local relative permittivity properties of the sample will lead to different tip-sample force gradients, which promote a shift Δf_0 in the tip oscillation frequency [20,21] which is, approximately,

$$\frac{\Delta f_0}{f_0} \cong -\frac{1}{2\,K}\,\frac{dF}{dz}, \tag{1}$$

where dF/dz is the tip-sample force gradient and K is the spring constant of the cantilever.

The tip-sample-substrate system configures a capacitor with the sample (wing) as part of the relative permittivity region, so the force among tip and substrate can be modeled as

$$F = -\frac{1}{2}\frac{\partial C}{\partial z}V_{dc}^2, \tag{2}$$

where C is the system capacitance and V_{dc} is the applied tip-sample bias.

From relations (1) and (2) we have:

$$\Delta f_0 \cong -\frac{f_0}{4K}\,\frac{d^2C}{dz^2}V_{dc}^2\ . \tag{3}$$

This equation relates the frequency shift Δf_0 with the applied bias voltage V_{dc}. The bias-independent term in equation (3) is defined as $\alpha_{\Delta f_0}$, given by

$$\alpha_{\Delta f_0}(Hz/V^2) \equiv \frac{f_0}{4K}\,\frac{d^2C}{dz^2}\,. \tag{4}$$

Since f_0, K and V_{DC} are well determined, local variations of the measured frequency shift Δf_0 are associated with changes in the capacitance second derivative in equations (3) and (4). The capacitance depends both on the geometry and on the relative permittivity of the medium, so we only need to use a suitable capacitive model to be able to determine the local relative permittivity of the sample from the EFM data.

The capacitor model applied here considers a conical tip and an infinite flat surface with relative permittivity ε_r and thickness h, which has a capacitance expressed as

$$C_{apex}(z) = 2\pi\varepsilon_0 R \ln\left(1 + \frac{R(1-\sin(\theta))}{z+\frac{h}{\varepsilon_r}}\right). \quad (5)$$

Inserting equation (5) into equation (4) leads to an expression from which the relative permittivity ε_r can be extracted:

$$\alpha_{\Delta f_0}(Hz/V^2) = \frac{\omega_0}{4k}\left[\frac{4\varepsilon_0\pi R^2(1-Sin(\theta))}{\left(\frac{h}{\varepsilon_r}+z\right)^3\left(1+\frac{R(1-Sin(\theta))}{\frac{h}{\varepsilon_r}+z}\right)}\right] - \frac{\omega_0}{4k}\left[\frac{2\varepsilon_0\pi R^3(1-Sin(\theta))^2}{\left(\frac{h}{\varepsilon_r}+z\right)^4\left(1+\frac{R(1-Sin(\theta))}{\frac{h}{\varepsilon_r}+z}\right)^2}\right] \quad (6)$$

where R is the tip apex radius, θ is the tip conical angle, z is the tip-sample distance, and h is the sample thickness. Figure 3 shows a scheme of the model, which is commonly applied for such configuration [12–16].

This capacitor model is valid within the following conditions: i) tip-sample distance z between 0 and 100 nm; ii) maximum sample thickness h around 100 nm; iii) sample relative permittivity ε_r smaller than ~ 100; iv) tip nominal radius R between 30 and 200 nm; v) tip cone angle θ between 10° and 45° [12].

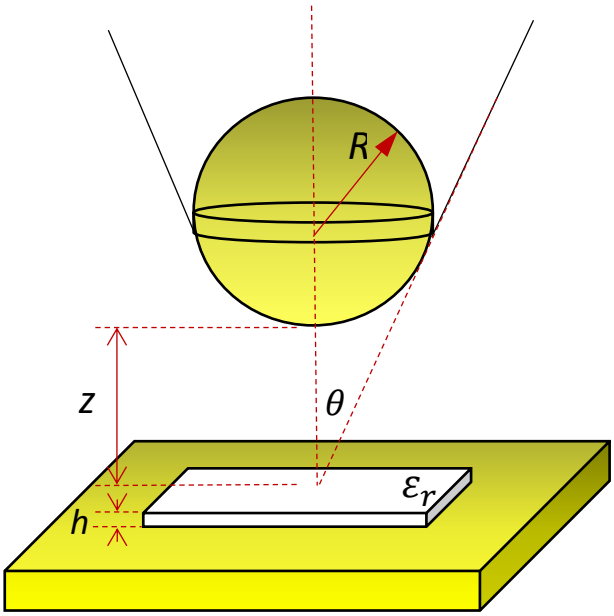

Figure 3: Capacitance model and parameters used in our calculations. *R* is the tip apex radius, θ is the tip conical angle, *z* is the tip-sample distance, *h* is the sample thickness and ε_r is the sample relative permittivity.

Determination of the coefficient $\alpha_{\Delta f_0}$

In the EFM mode, the microscope measures the frequency shift for each bias voltage in each position on the sample.

We varied the bias voltage from -10 V to +10 V, in steps of 1 V. Plotting the frequency shift as a function of bias voltage, we find a parabolical behavior, as can be seen in Figure 4. Fitting the data with the function

$$\Delta f_0 = \alpha_{\Delta f_0}(V_{dc} - V_{SP})^2 \ , \qquad (7)$$

where V_{SP} is the tip-sample surface potential difference due to their different work functions [20], we obtain the coefficient $\alpha_{\Delta f_0}$.

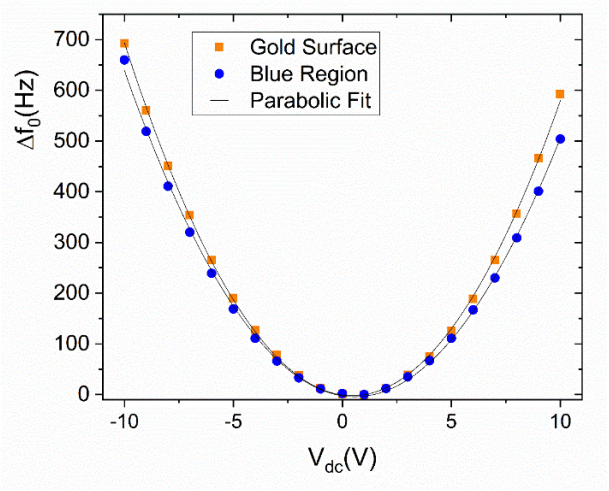

Figure 4: Frequency shift versus bias voltage of the gold surface (orange squares) and blue colored region of the wing (blue circles). The fitting using equation (7) results in $\alpha_{\Delta f_0}(gold) = (6{,}37 \pm 0{,}03) Hz/V^2$, and $\alpha_{\Delta f_0}(blue\ region) = (5{,}75 \pm 0{,}04) Hz/V^2$.

Construction of the relative permittivity map

From the AFM topography image, the thickness *h* is determined for each pixel, as shown in the Experimental section.

EFM measurements were carried out on the same sample region varying the bias voltage from -10 V to +10 V, resulting in 21 images, where each one is an array of frequency shift values. For the same pixel element in the sample image, we have 21 pairs of values: a frequency shift and its respective bias voltage. Through equation (7) we obtain an $\alpha_{\Delta f_0}$coefficient for each pixel element in the sample.

The parameters in equation (6), less the $\alpha_{\Delta f_0}$coefficient and the thickness *h*, are the same for all pixel elements.

Thus, solving for the relative permittivity of each pixel, we construct a relative permittivity map as can be seen in Figure 5.

Chalcopterix rutilans damselfly wings

Using the protocol described above, we constructed relative permittivity maps of the three colored regions: Red region (a), Blue region (b), and Yellow/Green region (c), as seen in Figure 5.

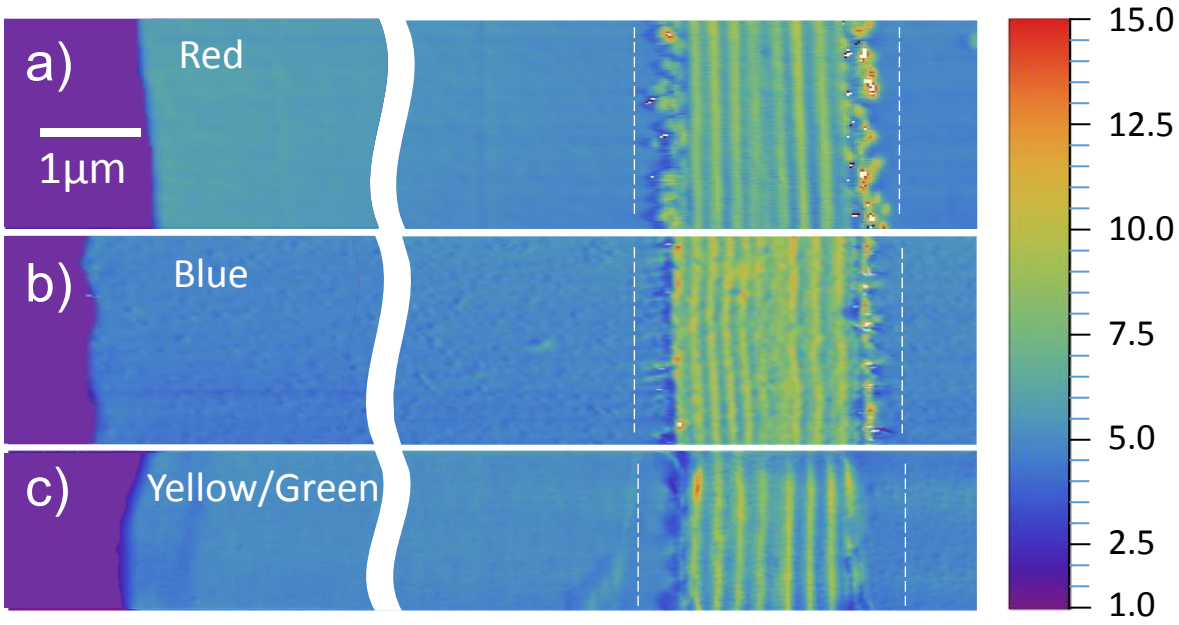

Figure 5: Relative permittivity image of three colored regions of the hind wings of *Chalcopterix rutilans*, Red region (a), Blue region (b), Yellow/Green region (c). The color scale on the right side gives the values of the relative permittivity. On the left side, with the purple color, we have the Au/Cr surface. The areas which appear bluish in the images ($\varepsilon_r \sim$ around 4) correspond to the polymerized resin wrapping the wing. The wing slice lies between the white vertical dashed lines which indicate the region where the profiles presented in Figure 6 were done.

The parameters used for the Red region are f_0 = 61.106 kHz, k = 1.19 nN/nm and *R* = (34.8 ± 0.2) nm; for the Blue region they are f_0 = 62.111 kHz, k = 1.87 nN/nm and

R = (42.6 ± 0.2) nm; and for the Yellow/Green region the parameters are f_0 = 67.972 kHz, k = 2.18 nN/nm and R = (35.9 ± 0.2) nm.

As done for the Al_2O_3 case (see Experimental Section), the substrate region was set with ε_r = 1since in this region there is only air between the probe and the gold substrate [15]. The polymerized resin in which the wing is mounted (see Experimental section) presents $\varepsilon_r(resin) \sim 4$. The cross-section cutting of the wing lies between the dashed lines, where the wing's nanometric layers can be seen. The wax layers that cover both sides of the wings appear as the more external discontinuous regions of the multilayered structure. The number of nanolayers and their thicknesses change from one colored region to another.

The ventral and dorsal sides shown in Figure 1 can be seen in cross-section in the images of Figure 5, where the ventral side is shown on the right, and the dorsal side on the left. On the left side of the Red region, the Blue region and the Yellow/Green region, each nanolayer thickness is (200 ± 9) nm, (150 ± 5) nm, and (185 ± 11) nm, respectively. In all colored regions, the layers on the right side are about (210 ± 10) nm thick, matching the ventral color, which is reddish for the whole of the ventral side of the wing, as seen in Figure 1b.

Figure 6 shows the average value of the relativity permittivity, for each colored region, along the cross-section of the wing (the area between the vertical white dashed lines in the figure). The values shown are obtained from an average along the vertical direction in Fig. 5, i.e., along each layer of the wing. The peaks and valleys indicate the modulation of the relative permittivity of the different wing constituent layers.

During the preparation of the wing samples, there is a variation of about 10 nanometers in the thicknesses of the slices. This variation has not impacted the results, as can be seen in Figure 6, which demonstrates the reliability of this technique for thin samples.

The relative permittivity of the layers ranges from 6 ± 1 to 8 ± 1. The main differences between the colored regions lie in the thickness and number of layers. Each multilayered structure is wrapped by a wax layer which is identified as the irregular region at the boundary of the wings in the maps of Figure 5, and as a valley in the relative permittivity profile with $\varepsilon_r(wax) \sim 4$ in Figure 6.

Using Time-of-Flight Secondary Ion Mass Spectrometry (TOF-SIMS), Carr *et al*.[18] concluded that the wing layer composition consists of mostly chitin with an alternating content of melanin, where chitin builds up the structure and melanin modulates the relative permittivity along the cross-section. From the results shown in Figure 6, we can see that, in addition, the number of layers and their thicknesses varies from one color region to the other. Comparing the composition of the layers measured in the TOF-SIMS study [18] with the relative permittivity maps of this work, we can say that melanin-rich layers have the relative permittivity around 8 ± 1, while low melanin concentration layers present a value around 6 ± 1.

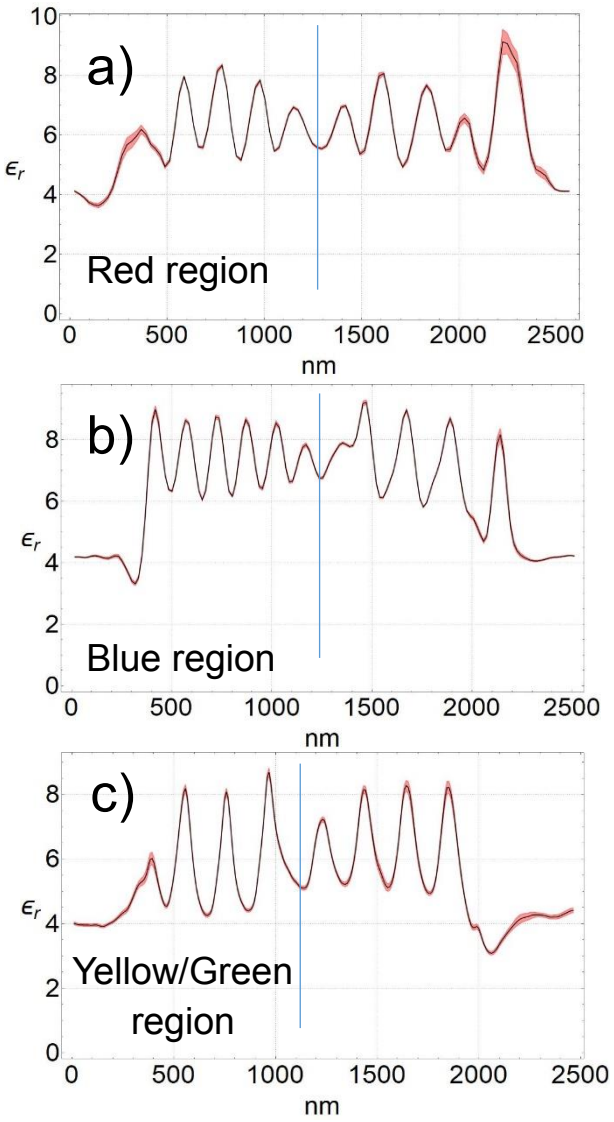

Figure 6 - The black curves show the profile of the relative permittivity of the cross-sections of the wing shown between the dashed lines in Figure 5. In a) the Red region, in b) the Blue region, and in c) the Yellow/Green region. The peaks and valleys correspond to the nanometric layers that constitute the wing. The dielectric constant of the peaks ranges between 8 and 9, and the valleys between 6 and 5. The red shadow on the curves show the standard error.

The structural color

As shown in Figure 1, the posterior wings of the male *Chalcopteryx rutilans* has a wide range of structural colors that covers almost the entire visible spectrum. We now seek to correlate the relative permittivity information obtained via EFM with the photonic behavior of the wing.

The wing has several layers with thicknesses comparable to the wavelength of light in the visible range. Through refraction and diffraction, which depend on the thicknesses and refractive indexes of the layers, the light wavelengths that will be reflected with higher intensities are selected, generating the displayed colors. As shown above (see Figures 5 and 6), the layers vary in quantity and thickness according to the colored region: the Blue region presents thinner layers, the Red region the thickest ones, and the Yellow/Green region has layers of intermediate thickness. It is interesting to note that for the Red region the thicknesses of the layers are about the same in the dorsal and ventral sides of the wing, consistent with the fact that the ventral side (Figure 1b) only shows red shades.

The profile of the refractive index in each colored region of the wing could, in principle, be directly obtained from the measured values of relative permittivity. However, the values obtained in the measurements of Figure 6 are of the static dielectric constant, $\varepsilon_r(\omega = 0)$, while for obtaining the values of the refractive index in the visible range one needs the values of the relative permittivity in the visible range, $\varepsilon_r(\omega \to \infty)$. For solid state cubic crystals, the two values are related by the Lyddane–Sachs–Teller relation [22], which gives the ratio $\varepsilon_r(0)/\varepsilon_r(\infty)$ in terms of the ratio between the squared values of the long-wavelength longitudinal and transverse optical phonons in the crystal. The Lyddane–Sachs–Teller relation has been extended to other crystalline systems and

disordered materials [23–25] but its application for the present case, chitin with a varying concentration of melanin, is not straightforward. In any case, there is a direct relation between the refractive indexes and the measured relative permittivity. Therefore, to simulate the optical reflectance of the damselfly wing, we consider that the refractive index varies along the cross section of each region of the wing following the continuous profiles shown in Figure 6, treating the minimum and maximum values of each profile as fitting parameters. The continuous profiles are discretized in layers thin enough to give a smooth as possible variation and then the transfer matrix technique is used to simulate the reflectance of the structure. This is actually a similar process as that used by Vukusic and Stavenga [6] and Stavenga *et al.* [7,8] except that in those works the spatial profile of the refractive index was taken to be proportional to the gray scale in TEM images, that is, it was assumed that the optical density is directly proportional to the electronic density. We consider our method to be more reliable since there is a direct relation between the relative permittivity and the refractive index.

Figure 7 shows the results of the simulation. On the left panels, the profile of the refraction indexes used to fit the optical reflectance are shown, for each colored region of the wing. As explained above, these are the same profiles obtained from the measurement of the relative permittivity, shown in Figure 6, only with the vertical scale changed for values of the refractive indexes; values chosen to fit the reflectance measurements. The right panels show the respective measured reflectances and the fittings obtained with the refraction index profiles shown on the left.

According to the results shown in Figure 7, the refraction index along the cross section of the damselfly wings vary from 1.52 ± 0.02 to 1.72 ± 0.02. The layers are essentially composed of chitin with varying melanin concentration from layer to layer, as discussed above, and these values are in good agreement with other determinations of chitin and melanin refractive indexes [8–10,26].

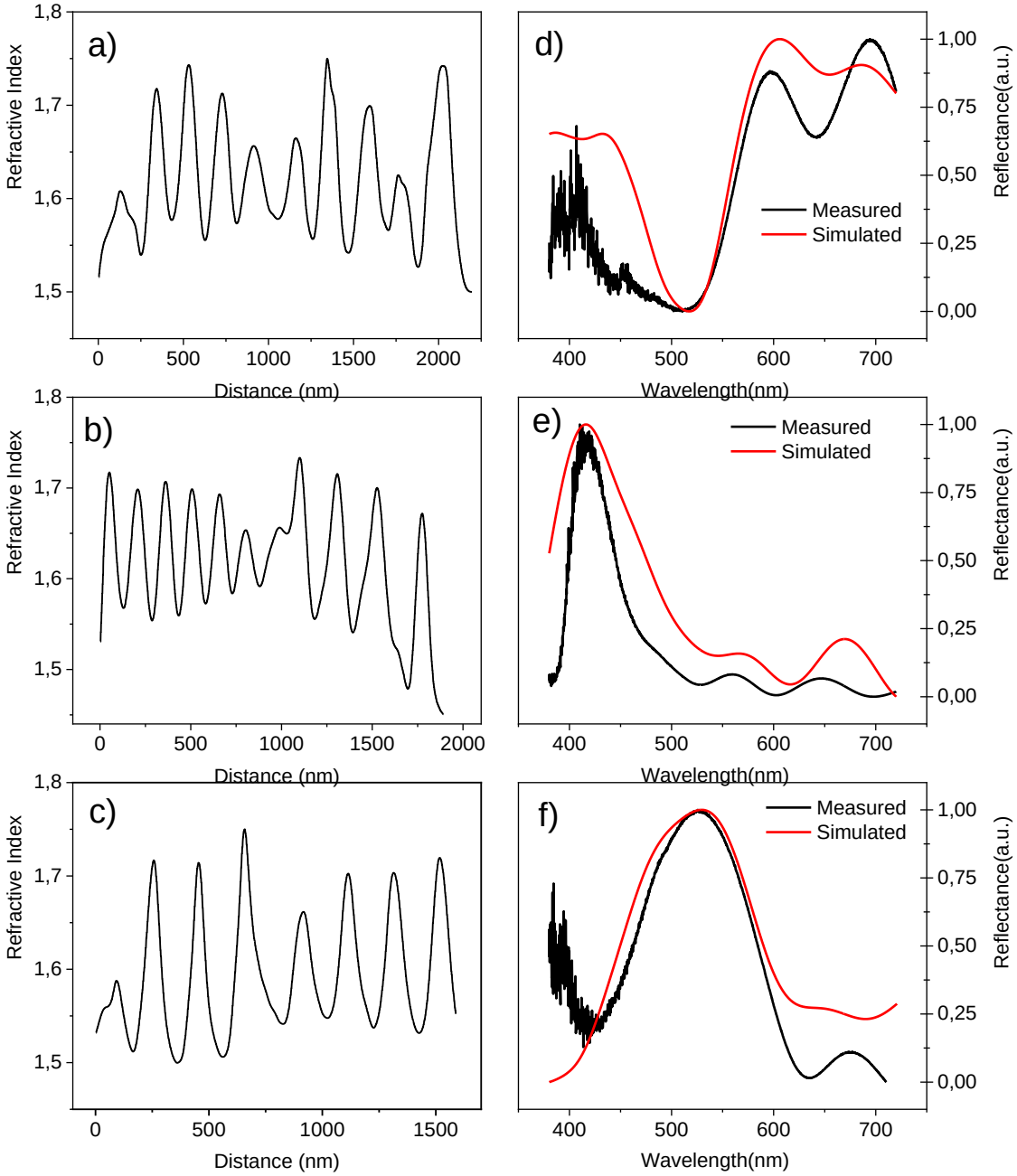

Figure 7: Panels on the left show the refractive index profile used in the simulation and those on the right the respective measured and simulated reflectance. In (a) and (d) we see the Red region, in (b) and (e) the Blue region, and in (c) and (f) the Yellow/Green region.

Conclusions

We have demonstrated that the Electrostatic Force Microscopy (EFM) technique is a reliable and useful tool to directly measure the relative permittivity of a natural photonic crystal. We showed how to obtain maps of the relative static permittivity with nanometric resolution, thus obtaining direct information about the internal structure of bio-systems and their dielectric properties in a nanoscale dimension. We applied the method to map the static relative permittivity of the cross-section of the posterior wing of the Amazonian damselfly *Chalcopteryx rutilans* and obtained the variation of the relative permittivity across the nanolayers which compose the wing. Since there is a direct relation between the static relative permittivity and the refractive index in the visible range of the electromagnetic spectrum, we were able to reliably reproduce the spatial variation of the refractive index across the wing and therefore simulate its optical reflectance. With this, we showed that the vivid colors displayed by the *Chalcopteryx rutilans* wings are due to the periodic change in the refractive index across the wing, which is therefore shown to be a one-dimensional natural photonic crystal. The different colors seen in different regions of the wing are due to the number and thicknesses of the constituent nanolayers in each different colored region, the refractive indexes in each colored region changing between approximately the same maximum and minimum values.

The direct relation between static relative permittivity and the visible refractive index means that the method demonstrated in this work is a reliable way of mapping the spatial profile of the refractive index of bio-nanostructured systems.

Experimental

Sample preparation

Damselfly wing samples were produced by ultramicrotomy. Fragments of the chosen colored region were embedded, with no previous cleaning procedure, in epoxy resin. The polymerized resin block was trimmed in a wedge shape, with the wing fragment section perpendicular to the wedge axis. Sections 40 nm thick of the apex wedge were cut using a diamond knife and placed on 10 mm x 10 mm Au/Cr coated silicon wafer pieces with 60 nm/20 nm film thickness, respectively. A conductive substrate surface is necessary for the proposed ε_r determination method. The sample also needs to be less than 100 nm thick to eliminate the influence of the stray capacitance [12]. Therefore, samples of three different color regions of the wing were prepared, namely Blue, Red and Green/Yellow ones.

An essential characteristic of the experiment is that both the sample and the conductive substrate need to be present within the AFM image. This is a key condition since the conductive substrate establishes a reference level in the analysis. Having both in the imaged region guarantees that the cantilever amplitude and, consequently, the effective radius of the tip will be the same for different materials, which is critical for the applied capacitor model [27]. Also, having the conductive surface and the sample in the same AFM image guarantees the precision in the determination of the thickness of the sample.

Determination of the parameters:

The sample thickness *h* is directly determined via AFM imaging. The microscope control software also determines the resonance frequency f_0 and the cantilever elastic constant *K*, using the Thermal tune method [28,29].

A critical parameter is the tip-sample distance *z*, that consists of the height H_{Lift} plus the cantilever amplitude Z_{amp}. The value of H_{Lift} is adjusted and presented by the microscope with remarkably high accuracy and precision. The value of Z_{amp} is obtained by the standard amplitude-distance curve method.

Another critical parameter is the effective radius *R*. To obtain it, we carry out EFM measurements on the gold surface and determine the coefficient $\alpha_{\Delta f_0}$. Over the gold surface, the effective thickness of the sample *h* goes to zero, thus $\frac{h}{\varepsilon_r} = 0$ [13,30], and equation (6) can be seen as a function of *R*.

The coefficient $\alpha_{\Delta f_0}$ depends on *z* and to obtain the correct *R*, it is necessary to perform the EFM measurements of the sample and the substrate with the same height reference. EFM measurements with both the substrate and sample in the same image solve this issue.

The conical angle is θ = 0.261 rad, as informed by the tip producer. We used the AC240TM-R3 probe model by Oxford Instruments Asylum Research in all measurements.

Al_2O_3 reference sample

We made reference samples of a material with a well-known relative permittivity. In this way, applying the method to this reference sample, we validated the technique presented in this paper to measure the relative permittivity of the nanostructures in the damselfly wings.

Our reference samples were photolithographically defined 5 µm radius disks of Al_2O_3 films deposited by ALD on Au/Cr coated silicon wafer pieces with 60 nm/20 nm thicknesses, respectively.

The topographic image of an Al_2O_3 disk by AFM is shown in Figure 8a. The sample thickness was (21.0 ± 0.2) nm, referred to the gold surface.

In the EFM mode, the microscope measures the frequency shift for each bias voltage in each position on the sample. We varied the bias voltage from -10 V to +10 V, in steps of 1 V. Plotting the frequency shift versus bias voltage, we obtain a parabolical behavior. Fitting the data with equation (7) we obtain the $\alpha_{\Delta f_0}$ coefficient. Doing this operation for each pixel we build the image of alpha coefficients as we can see in Figure 8b.

The gold surface has a higher $\alpha_{\Delta f_0}$ coefficient than the Al_2O_3 disk, Figure 8b. This means that the frequency shifts on gold are larger for all bias voltages, so the tip-substrate interaction on the gold surface is stronger than on the alumina disk.

The tip radius was obtained using the $\alpha_{\Delta f_0}$ coefficient for measurements on the gold surface for h = 0, and was R = (36.7 ± 0.2) nm, Figure 8b. The tip-sample distance z is 44 nm, determined by the sum of 40 nm of the setup lift height with the 4 nm of the cantilever oscillation amplitude [16]. We choose a small cantilever oscillation amplitude

during the EFM measurements in order to keep the tip not far from the sample surface, in a range where this method is valid [12].

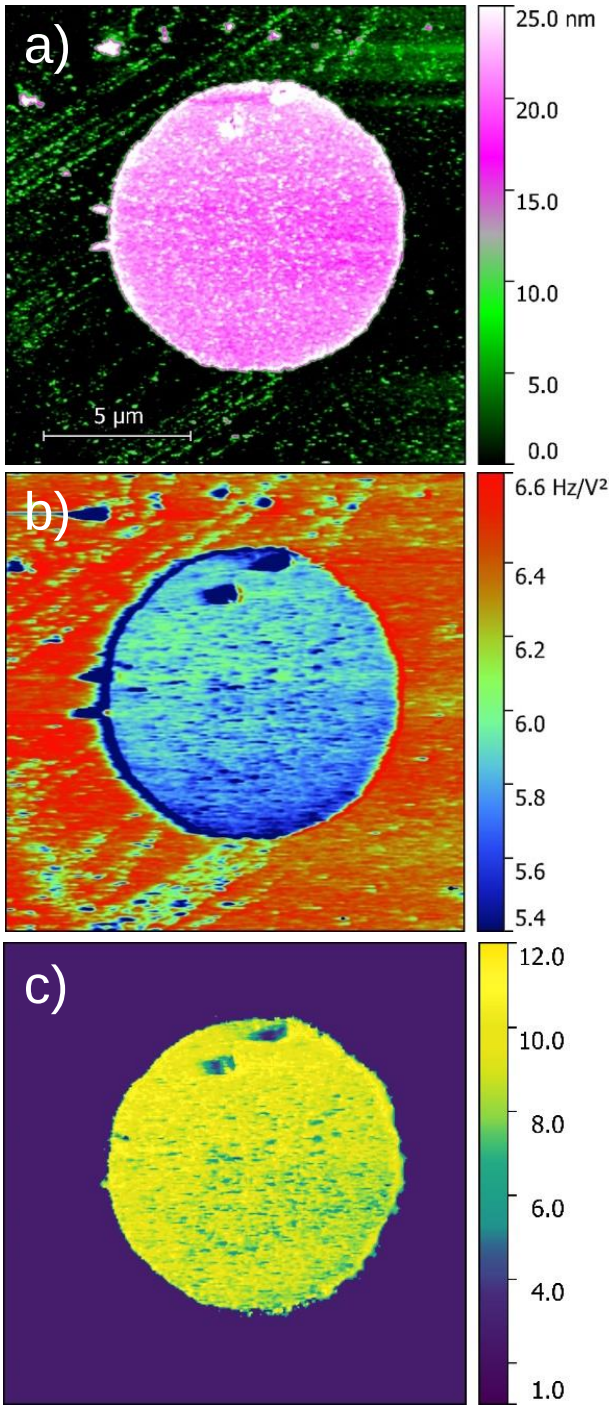

Figure 8: Thickness measurement of the Al_2O_3 disk a), map of the $\alpha_{\Delta f_0}$ coefficient b), and dielectric constant map of the alumina film disk on gold c).

The free oscillating frequency f_0 = 73.403 kHz and the cantilever elastic constant *k* = 2,24 nN/nm, were calculated using the Thermal tune.

The height *h*, Figure 8a, and the $\alpha_{\Delta f_0}$ coefficient, Figure 8b, are different for each pixel in the sample, the other parameters mentioned above and seen in equation 6 are the same for all pixels. Solving equation (6) for ε_r we constructed the map of the dielectric constant as shown in Figure 8c. In the reconstructed dielectric image, the region corresponding to the substrate was set to $\varepsilon_r = 1$ since this region corresponds to the air relativity permittivity [15].

We obtained $\varepsilon_r(Al_2O_3) = 9{,}3 \pm 0{,}2$, which is an agreement with the value obtained by Yota *et al.*, ε_r = 9.2 [31], and Biercuk *et al*., ε_r= 9 [32], both results being from Al_2O_3 produced by ALD, and also with the reference value for the dielectric constant of Al_2O_3 reported in several handbooks [33].

Reflectance measurements

For measurements of the reflectance spectra, a halogen lamp with a color temperature of 3200 K (OLS1 FIBER ILLUMINATOR, Thorlabs) was used, which allows reflection measurements in the spectral range from 350 nm to 1100nm. A set of biconvex lenses focused the source light on the desired colored region and another set of biconvex lenses delivered the reflected light to an optical fiber with 0.22 numerical aperture. The light was delivered through this optical fiber to the spectrometer (USB4000, Ocean Optics). Spectral data were acquired with the Spectra Suite software (Ocean Optics). Spectral measurements were made in three colored regions of male damselfly hind wings, namely Yellow/Green, Red, and Blue region. In this work we study the light captured at 60º in relation to the normal of the wing.

Acknowledgments

The authors would like to thank Prof. Angelo Machado for his generosity and enthusiasm for this work, supplying us with the precious specimens of damselflies studied here. We acknowledge the Center of Microscopy at the Universidade Federal de Minas Gerais for providing the equipment and technical support for experiments involving electron and scanning probe microscopies.

Funding

The financial support of the agencies FAPEMIG, CNPq, CAPES, and FINEP allowed this research to be realized.

REFERENCES

1. Malmivuo, J.; Plonsey, R. *Bioelectromagnetism: Principles and Applications of Bioelectric and Biomagnetic Fields*; Oxford University Press: Oxford, U.K., 2012. doi:10.1093/acprof:oso/9780195058239.001.0001
2. Warshel, A.; Sharma, P. K.; Kato, M.; Parson, W. W. *Biochim. Biophys. Acta - Proteins Proteomics* **2006**, *1764*, 1647–1676. doi:10.1016/j.bbapap.2006.08.007
3. Crovetto, A.; Huss-Hansen, M. K.; Hansen, O. *Sol. Energy* **2017**, *149*, 145–150. doi:10.1016/j.solener.2017.04.018
4. Joannopoulos, J. D.; Johnson, S. G.; Winn, J. N.; Meade, R. D. *Photonic Crystals*; Princeton University Press: Princeton, USA, 2011. doi:10.2307/j.ctvcm4gz9
5. Vukusic, P.; Sambles, J. R. *Nature* **2003**, *424*, 852–855. doi:10.1038/nature01941
6. Teyssier, J.; Saenko, S. V.; Van Der Marel, D.; Milinkovitch, M. C. *Nat. Commun.* **2015**, *6*, 1–7. doi:10.1038/ncomms7368
7. Vukusic, P.; Stavenga, D. G. *J. R. Soc. Interface* **2009**, *6*, S133-48. doi:10.1098/rsif.2008.0386.focus
8. Stavenga, D. G.; Leertouwer, H. L.; Hariyama, T.; De Raedt, H. A.; Wilts, B. D. *PLoS One* **2012**, *7*, 1–8. doi:10.1371/journal.pone.0049743
9. Stavenga, D. G.; Wilts, B. D.; Leertouwer, H. L.; Hariyama, T. *Philos. Trans. R. Soc. Lond. B. Biol. Sci.* **2011**, *366*, 709–723. doi:10.1098/rstb.2010.0197
10. Nixon, M. R.; Orr, a G.; Vukusic, P. *Opt. Express* **2013**, *21*, 1479–1488. doi:10.1364/OE.21.001479

11. Gabriel, C.; Gabriel, S.; Corthout, E. *Phys. Med. Biol.* **1996**, *41*, 2231–2249. doi:10.1088/0031-9155/41/11/001

12. Gomila, G.; Toset, J.; Fumagalli, L. *J. Appl. Phys.* **2008**, *104*, 024315. doi:10.1063/1.2957069

13. Gramse, G.; Casuso, I.; Toset, J.; Fumagalli, L.; Gomila, G. *Nanotechnology* **2009**. doi:10.1088/0957-4484/20/39/395702

14. Fumagalli, L.; Ferrari, G.; Sampietro, M.; Gomila, G. *Appl. Phys. Lett.* **2007**, *91*, 243110. doi:10.1063/1.2821119

15. Fumagalli, L.; Ferrari, G.; Sampietro, M.; Gomila, G. *Nano Lett.* **2009**, *9*, 1604–1608. doi:10.1021/nl803851u

16. Riedel, C.; Arinero, R.; Tordjeman, P.; Ramonda, M.; Ĺvque, G.; Schwartz, G. A.; De Oteyza, D. G.; Alegria, A.; Colmenero, J. *J. Appl. Phys.* **2009**, *106*, 1–6. doi:10.1063/1.3182726

17. Valeriano, W. W. Cores Estruturais Da Asa Da Libelula Chalcopteryx Rutilans, Universidade Federal de Minas Gerais, Brazil, 2015, MSc dissertation, available at https://www.fisica.ufmg.br/posgraduacao/defesas/mestrado-2015-wescley-valeriano/

18. Carr, D. M.; Ellsworth, A. A.; Fisher, G. L.; Valeriano, W. W.; Vasco, J. P.; Guimarães, P. S. S.; de Andrade, R. R.; da Silva, E. R.; Rodrigues, W. N. *Biointerphases* **2018**, *13*, 03B406. doi:10.1116/1.5019725

19. Resende, D. C.; De Marco Jr., P. *Rev. Bras. Entomol.* **2010**, *54*, 436–440. doi:10.1590/S0085-56262010000300013

20. Weiss, P. S. *J. Am. Chem. Soc.* **2001**, *123*, 9725–9725. doi:10.1021/ja015224b

21. Sarid, D.; Coratger, R.; Ajustron, F.; Beauvillain, J. *Microsc. Microanal. Microstruct.* **1991**, *2*, 649–649. doi:10.1051/mmm:0199100206064900

22. Lyddane, R. H.; Sachs, R. G.; Teller, E. *Phys. Rev.* **1941**, *59*, 673–676.

doi:10.1103/PhysRev.59.673

23. Sievers, A. J.; Page, J. B. *Infrared Phys.* **1991**, *32*, 425–433. doi:10.1016/0020-0891(91)90130-8

24. Schubert, M. *Phys. Rev. Lett.* **2016**, *117*, 215502. doi:10.1103/PhysRevLett.117.215502

25. Noh, T. W.; Sievers, A. J. *Phys. Rev. Lett.* **1989**, *63*, 1800–1803. doi:10.1103/PhysRevLett.63.1800

26. Leertouwer, H. L.; Wilts, B. D.; Stavenga, D. G. *Opt. Express* **2011**, *19*, 24061. doi:10.1364/oe.19.024061

27. Hudlet, S.; Saint Jean, M.; Guthmann, C.; Berger, J. *Eur. Phys. J. B* **1998**, *2*, 5–10. doi:10.1007/s100510050219

28. Hutter, J. L.; Bechhoefer, J. *Rev. Sci. Instrum.* **1993**, *64*, 1868–1873. doi:10.1063/1.1143970

29. Butt, H. J.; Jaschke, M. *Nanotechnology* **1995**, *6*, 1–7. doi:10.1088/0957-4484/6/1/001

30. Sacha, G. M.; Sahagún, E.; Sáenz, J. J. *J. Appl. Phys.* **2007**, *101*, 024310. doi:10.1063/1.2424524

31. Yota, J.; Janani, M.; Banbrook, H. M.; Rabinzohn, P.; Bosund, M. *J. Vac. Sci. Technol. A* **2019**, *37*, 050903. doi:10.1116/1.5112773

32. Biercuk, M. J.; Monsma, D. J.; Marcus, C. M.; Becker, J. S.; Gordon, R. G. *Appl. Phys. Lett.* **2003**, *83*, 2405–2407. doi:10.1063/1.1612904

33. Nanni, P.; Viviani, M.; Buscaglia, V. Synthesis of Dielectric Ceramic Materials. In *Handbook of Low and High Dielectric Constant Materials and Their Applications*; Hari Singh Nalwa, Ed.; Academic Press: Ibaraki, Japan, 1999; pp 429–455. doi:10.1016/B978-012513905-2/50011-X